Optical Engineering

OpticalEngineering.SPIEDigitalLibrary.org

Polarization insensitive performance of randomly structured antireflecting planar surfaces

Abigail Peltier
Gopal Sapkota
Jason R. Case
Menelaos K. Poutous

SPIE.

Abigail Peltier, Gopal Sapkota, Jason R. Case, Menelaos K. Poutous, "Polarization insensitive performance of randomly structured antireflecting planar surfaces," *Opt. Eng.* **57**(3), 037109 (2018), doi: 10.1117/1.OE.57.3.037109.

Polarization insensitive performance of randomly structured antireflecting planar surfaces

Abigail Peltier,* Gopal Sapkota, Jason R. Case, and Menelaos K. Poutous
University of North Carolina at Charlotte, Department of Physics and Optical Science, Charlotte, North Carolina, United States

Abstract. The transmittance polarization extinction ratio of fused silica substrates with random antireflective surface structures (rARSS) was investigated. The antireflective structures were etched on both sides of the substrates to suppress Fresnel reflection from the two surfaces, and the substrates were processed with three different sets of etching parameters, resulting in samples with three distinct sets of surface characteristics. In addition, three of the samples were fabricated with identical processes on both sides, while one was fabricated with a different process on each side. Normal incidence transmission spectra, spanning wavelengths from 300 to 1900 nm, are presented for each double-sided substrate, and variable angle of incidence polarization measurements were taken at 633 nm. Although the spectral Fresnel reflection suppression of all of the samples was measured to similar levels at normal incidence, the polarized transmittance response was found to vary considerably, correlating with the surface morphology differences and the front-to-back surface roughness similarities between the samples. Polarization insensitivity was verified from normal incidence to Brewster's angle. Comparisons with the ideal single-layer thin-film antireflection coating performance calculations show that rARSS samples are polarization insensitive over a larger range of angles and have a wide wavelength band of transmission enhancement. [DOI: 10.1117/1.OE.57.3.037109]

Keywords: subwavelength structures; optical properties; optical materials; thin films; polarization; antireflection coatings.

Paper 171966P received Dec. 8, 2017; accepted for publication Feb. 28, 2018; published online Mar. 21, 2018.

1 Introduction

Fresnel reflectivity at the surface of optical components, due to the refractive index mismatch between the bulk material and ambient, is a considerable issue for optical systems. In various applications such as flat panel displays, high-performance lenses, photovoltaic devices, screens of mobile electronic devices, and superluminescent diodes, it is essential to reduce unwanted reflections to increase performance of optical systems.[1] Conventional single-, double-, and multilayered thin-film antireflection coatings (ARC) can suppress Fresnel reflections to nearly zero.[2] Random antireflecting surface structures (rARSS) fabricated directly on a substrate surface have been shown to considerably reduce Fresnel reflectivity as well.[3] The performance of rARSS is understood as a gradient-index transition between two optical media, caused by the gradual electromagnetic wave transition between the ambient and substrate volumes.[4] The rARSS gradient refractive index model is based on the subwavelength surface-feature scale and the random-feature surface morphology. These structures have measurable spectral and directional antireflective (AR) properties. The random surface structures are made of the same material as the substrate, resulting in similar physical properties to that of the bulk material. As a result, such structures can perform well at high incident light energies and have been reported to withstand environmental and erosive tests.[5–10]

In general, reduction in Fresnel reflectivity can be achieved using optical boundary engineering. Some commonly used methods include conventional thin-film layers, ordered subwavelength-scale microstructures, random subwavelength-textured layers, and gradient optical-index layers.

Quantitative analysis and simulations of the optical performance of these boundaries are based, respectively, on stratified media interference,[11] subwavelength grating evanescent mode coupling,[12] effective-media approximations (EMA),[13] and gradient-index wave propagation.[14,15] In all cases, scattering away from the specular light-propagation direction is considered minimal for the wavelengths of interest since the transmitted optical power through the passive boundary is higher than the value without an antireflective treatment. For the rARSS layer, since the subwavelength features are random in both their transverse and longitudinal directions (width and height), EMA analysis is based on an effective density function, which is used to determine the average refractive index of the layer, with an effective depth of the order of the incident wavelength. Another quantitative analysis approach is to combine sequential EMA layers to approximate a slowly increasing index profile from the ambient to the substrate boundary index.

Random structure fabrication processing found in the literature varies,[16–18] with normal incidence transmission measurements having similar spectral performance for feature distributions that are morphologically very different. Because of this, angle-of-incidence (AOI) measurements are most useful to identify performance differences between rARSS samples with different structural density functions.

In this paper, we present normal incidence transmission spectra from 300 to 1900 nm and variable AOI polarization measurements taken at 633 nm, for double-sided processed rARSS substrates. Substrates were processed on both sides

*Address all correspondence to: Abigail Peltier, E-mail: apeltier@uncc.edu

0091-3286/2018/$25.00 © 2018 SPIE

to reduce Fresnel reflection from all of the substrate boundaries, to eliminate the polarization signature of an unprocessed boundary from the variable AOI polarization measurements, and to ensure that there would be no total internal reflection caused by an unprocessed boundary's critical angle. Three different sets of etching parameters were used to process the substrates, resulting in samples with three distinct sets of surface characteristics. We characterized morphologically the rARSS on the fused silica (FS) substrate surfaces for each of the three parameter sets and used this to understand the differences in AR performance among the samples. Three of the samples were fabricated with identical processes on both sides while one was processed with dissimilar processes on each side. This allowed us to explore how the similarity of the front and back surface morphology impacts the overall transmission of polarized light. The testing protocol is presented in the following section. The results are presented and discussed in Sec. 3; it is shown that samples with dissimilar subwavelength features on the front and back sides will exhibit polarization insensitivity over a smaller range of incident angles than similarly processed samples with identical features on both sides. It is also shown that samples with different subwavelength features may show similar transmission enhancement performance at normal incidence but will have different polarization insensitivity properties when transmission is examined at varying AOI. We measured the transmission enhancement at normal incidence and the normalized transmission for *s* and *p* polarizations from 0 deg to 75 deg AOI. In all cases, these measurements were compared with plain FS identical unprocessed substrates. The measured polarization extinction ratio was compared with results from simulations of an ideal single-layer thin-film ARC. A Bruggeman EMA model[19,20] was used to simulate the rARSS boundaries, resulting in good agreement with the experimental measurements of the polarization extinction ratio.

2 Experimental Design

FS substrates were used after immersion in a Piranha cleaning solution[21] for 1 h, followed by a deionized water rinse and subsequent drying with flowing nitrogen gas. A thin discontinuous layer of Au (<20 nm) was deposited on all of the substrates at once, using an AJA International Inc., sputter deposition system (ATC 1800-F). Very thin sputtered Au films tend to be nonuniform and in many cases discontinuous.[22,23] For our application, the randomness of the Au film is used to "seed" the random etch process as a partial "perforated" mask. The coating thickness listed above is more of an estimated average across the substrate surface. While we previously reported on work in which rapid thermal annealing of the Au layer was utilized as an etch mask,[24] in the present work, the Au layer was not annealed and the rARSS on FS were fabricated by a reactive-ion etch plasma using a mixture of SF_6 and O_2 as the process gases. The etching conditions were adjusted to obtain three distinct etched feature profiles of rARSS.[25] The recipes were multiplexed with various substrate surfaces, as shown in Table 1. The recipe used to process both sides of sample A was taken arbitrarily as the comparison baseline recipe. There was no optimization of the optical transmission enhancement as the experimental trials were used to induce slightly different characteristics on the optical surfaces, around an already-established process. One surface of sample C was processed using recipe I and the other using recipe III to produce a nonsymmetric rARSS window.

Table 1 Fabrication process experimental design for rARSS on FS substrates.

Process Variant	Side 1 of substrate	Side 2 of substrate	Plasma power	Gas flow rate	Etch time
I	A	A,C	Baseline	Baseline	Baseline
II	B	B	+20%	−20%	Baseline
III	C,D	D	−5%	+20%	+30%

The structural and morphological study of the fabricated rARSS used a Raith 150 scanning electron microscope (SEM). Figure 1 shows high-resolution (2048 × 1536 pixel) top-down, surface gray-scale images of the processed substrates, obtained at 50,000 times magnification, with a constant working distance and accelerating voltage for all images. The gray-scale had 256 gray levels. The images were analyzed using a granulometry routine,[26] but they were first put through an image processing routine that consisted of median-gray-value thresholding, to ensure that brightness and contrast differences during imaging would not skew the granulometry results. The bright pixel clusters in the images indicate elevated features, i.e., silica islands, whereas the dark clusters identify voids. Islands and voids were classified separately, using gray-scale inversion of the images and counting the granule populations independently. The granules used for classification were octagons, varying from 5 to 100 pixels in diagonal and scaled to the dimensional bar for each SEM image. Multiple areas of each surface were imaged, and the results were averaged, per surface and process condition. The resulting granule pattern spectrum $\Phi(k)$ and its derivative $d\Phi(k)$, for both islands and voids of diagonal dimension k were computed, to obtain the FS density distribution by granule (feature) and the granule size histogram populations, respectively. The difference of island to void distribution: $\Phi_{\text{islands}}(k) - \Phi_{\text{voids}}(k)$, and the population difference of islands to voids: $d\Phi_{\text{islands}}(k) - d\Phi_{\text{voids}}(k)$, were calculated to identify the effective density of FS in the imaged surfaces and the feature size dominance. Although the granulometry of the SEM surface images does not contain depth information, it yields transverse-dimension feature sizes that are used in the EMA model construction.

Spectral transmission measurements from 300 to 1900 nm at normal incidence were made through the center of the samples, using a Cary 5000 (Varian) ultraviolet-visible-near-infrared dual-beam grating spectrophotometer. The normal incidence ($\theta = 0$ deg) transmittance of the rARSS samples T_{ARSS} was normalized to the respective measured transmittance of plain polished FS substrates T_{FS}, and the spectral transmission enhancement was calculated using the relation

$$\tau(\lambda, \theta = 0) = \tau_o(\lambda) = \left[\frac{T_{\text{ARSS}}(\lambda, 0)}{T_{\text{FS}}(\lambda, 0)} - 1\right]. \quad (1)$$

The dimensionless quantity $\tau(\lambda, \theta)$ is the fractional increase in transmittance above the unprocessed FS values

for values of $\tau > 0$ and a decrease in transmittance for $\tau < 0$. For FS optical components, since the Fresnel losses per interface are an average of -3.7% of the incident intensity in the spectral region of interest, the total maximum transmission enhancement is an average of $+7.2\%$, accounting for both substrate surfaces.

Additionally, *s*- and *p*-polarized incident light transmission was measured as a function of AOI, using a Schmitt Industries, Inc. (Portland, Oregon) CASI scatterometer. All processed (rARSS) samples and plain polished FS samples were measured to obtain the degree of polarization per AOI. The CASI uses a 633-nm HeNe laser source, aligned through the center of the sample, and measures the transmitted power with a detector on a goniometer arm. The beam spot size was 3 mm at the sample's entry surface for all tests. The CASI system has a typical noise-equivalent bidirectional transmissive distribution function of 5.00 (10^{-8}), through use of variable apertures and detector bias conditions. The samples were tested multiple times and in multiple locations, and the results were averaged. The AOI was varied from 0 deg to 75 deg, in intervals of 0.1 deg, using the automated sample stage of the CASI system. Measurements at angles >75 deg were not possible due to the obstruction of the beam path by the sample stage holder. To provide a comparison independent of the test apparatus, a plain FS substrate, without any AR treatment, was used as the baseline sample. The transmittance versus AOI was measured for both polarization states with the plain sample, and these values were used to compute the transmission enhancement ratios and polarization coefficient ratios from the rARSS samples. The polarization extinction transmission ratio[27] deviation from unity was calculated as a measure of polarization independence

$$e_T(\theta) - 1 = \left[\frac{T_p(\theta)}{T_s(\theta)} - 1\right], \tag{2}$$

where θ is the value of the AOI. The quantity in Eq. (2) is zero for equal values of the transmitted polarized intensities and is nonzero otherwise. Because the polarization extinction ratio is a ratio of two measured transmittances (*p* over *s* polarizations), both taken using the same apparatus, and not a ratio of a measured quantity over a computed one or a reference substrate, the "tool signature" is minimized. Positive values resulting from use of Eq. (2) indicate that the *p*-polarized incident light has a higher transmission than the *s*-polarized component, which is always true for bare substrates, as the AOI approaches the value of Brewster's angle.

To compare the measured performance of the rARSS on FS samples to a baseline, we performed numerical simulations of the ideal single-layer ARC. The ideal single-layer ARC consists of a perfect index-matched single-layer film (PAR), with a refractive index chosen as the square-root of the substrate index value at 633-nm wavelength. The simulations consisted of fully dispersive spectral transmittance calculations at normal incidence, with the coatings on both sides of the FS substrate. The transmission enhancement was computed using Eq. (1), with plain FS as the normalization. To compare the ideal ARC simulations with the experimental polarization extinction results, simulations were performed for both polarization orientations with variable AOI at 633 nm. The polarization extinction ratio deviation from unit-value was calculated and compared with the experimental results. The scalar matrix propagation method was used for all simulations.[28]

3 Results and Discussion

The granule pattern normalized spectra $\Phi(k)$ and their derivatives $d\Phi(k)$ were calculated for both islands and voids of diameter k, using SEM images similar to the ones shown in Fig. 1. These two quantities correspond, respectively, to the discrete probability distribution function of the respective features and the discrete feature spectrum (histogram). Both feature-type distribution functions are bound by the condition

$$\Phi_{\text{islands}}(k) + \Phi_{\text{voids}}(k) \leq 1. \tag{3}$$

The equality is true only for $k = \infty$, meaning that, when all feature diameters are counted, the SEM image balance of islands to voids is obtained. At some value $k_{\max}$, the counting will not yield new features, and the granulometry will stagnate. Conversely, if feature sizes smaller than $k_{\min}$ do not exist, the population count will not start. This condition does

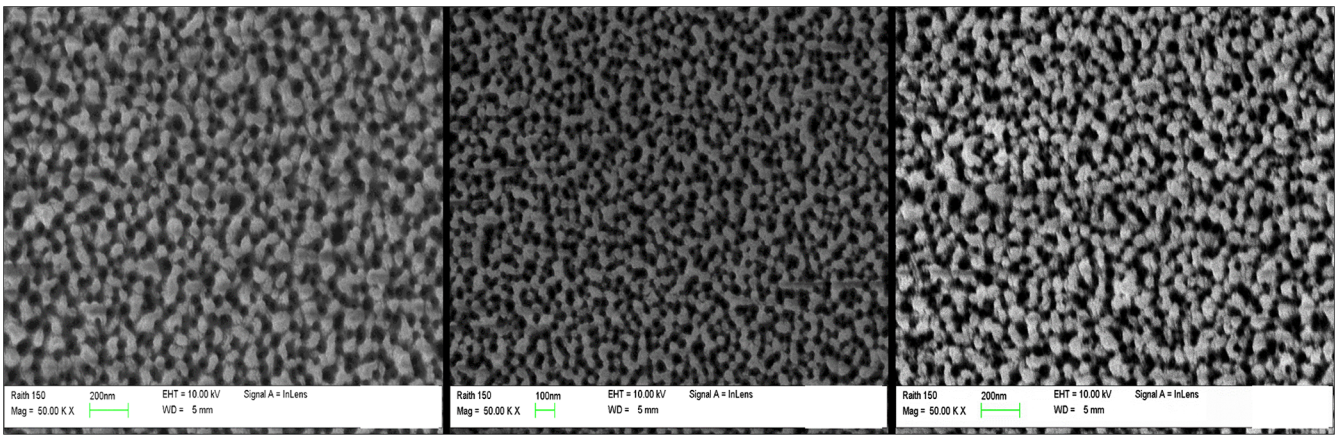

(a) (b) (c)

Fig. 1 SEM micrographs of the random structure AR boundary from the FS substrates tested, showing the top-down view of the rARSS. The identifiers (a, b, and c) correspond to the process variants listed in Table 1. All micrographs displayed are at 50,000 times magnification.

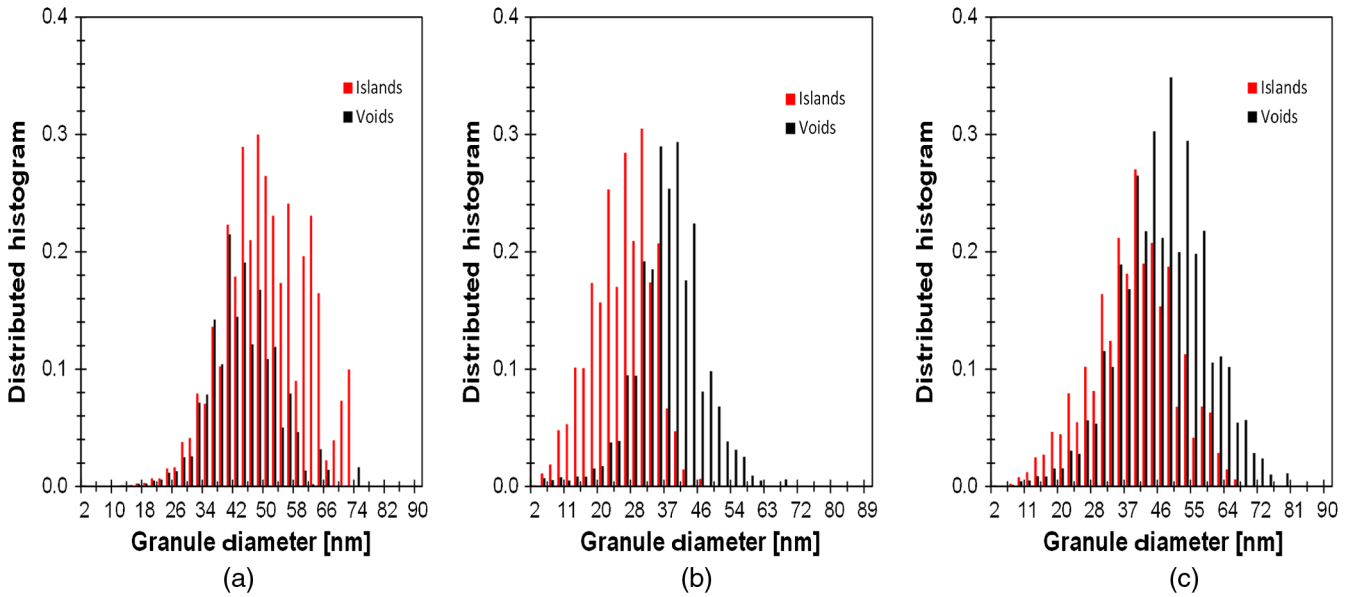

Fig. 2 Distributed histograms of voids (in black) and islands (in red) from the feature sizes corresponding to the SEM micrographs of the random structure AR boundaries shown in Fig. 1. The identifiers (a, b, and c) correspond to the measured process types from Table 1. The histograms were computed using granulometry.

not imply any type of interdependence of the distributions, which are totally independent variables. In turn, the feature spectrum is peaked at the mean value of each normalized distribution function, i.e.,

$$d\Phi(k) \leq d\Phi(k_{\text{mean}}), \tag{4}$$

where

$$\Phi(k_{\text{mean}}) = \frac{1}{2}\Phi(\infty). \tag{5}$$

The product of each population distribution with the corresponding feature spectrum $\Phi(k)d\Phi(k)$, for each process variant is shown in Fig. 2. We chose to use the product of the granulometry results instead of the individual values to "weigh" the population histograms with the population distributions. The resulting distributed histogram displays the feature sizes and the feature balance in a compact form. The mean value of each feature of interest is indicated by the histogram peak, with the population balance as the ratio of the two population mean values. Dominance of a certain feature size over the other is indicated by the bar ratios at the specific granule size. Figure 2(a) shows that process-I produces a large density of large FS islands, with a mean diameter of 48 nm and a coverage density of 60% of the surface measured. FS islands with smaller diameters are "balanced" with equal size voids; however, void sizes decrease considerably for larger granules, indicating a surface that is 60% FS and 40% air. Process-II [Fig. 2(b)] results have a different trend: larger voids surround smaller islands, with mean diameters of 39 and 30 nm, respectively, and a 50%–50% coverage density. The trend of process-III indicates that the voids are larger than the FS islands, with a coverage density of 56% void to 44% FS and mean diameters of 48 and 40 nm, respectively. The feature populations in processes-I and II are more segregated, whereas the populations of process-III are similar and have a larger breath.

The morphological differences of the three types of surfaces fabricated can also be quantified as actual differences between the constituent population normalized distributions $\Phi(k)$ and the differences of the products: $\Phi(k)d\Phi(k)$, shown in Fig. 3. Figure 3(a) shows the differential weighted-population $[\Phi_{\text{islands}}(k)d\Phi_{\text{islands}}(k) - \Phi_{\text{voids}}(k)d\Phi_{\text{voids}}(k)]$ evolution, and Fig. 3(b) shows the population differential normalized distribution $[\Phi_{\text{islands}}(k) - \Phi_{\text{voids}}(k)]$, with respect to granule size. The differential population shows that all three processes have generated distinct FS features; in process-I the predominance is FS islands (positive differential), process-II has a feature population balance in numbers, and process-III has more voids. The differential distribution results [Fig. 3(b)] indicate that process-I has a balanced distribution of feature diameters from 2 to 42 nm, and from 44 to 76 nm it is predominantly a population of FS islands. In contrast, process-III has a few small (< 40 nm) islands in excess of voids, with a higher density of voids for larger granules. Process-II is a mix of many small FS islands, which is a "sea" of medium size voids (42 to 60 nm). Combining the results shown in Figs. 2 and 3, the transverse morphological constitution of the FS rARSS boundaries is quantified.

To provide a performance comparison, the spectral transmission of unprocessed FS substrates at normal incidence was measured and averaged to compute transmission enhancement of the rARSS surfaces [Eq. (1)]. Figure 4 shows the transmission enhancement at normal incidence for the simulated ideal PAR and the measured double-side etched FS samples A, B, C, and D listed in Table 1. The results are compared with the theoretical maximum transmission for a plane FS substrate. Realistically, the PAR is unattainable as the material for the ideal index-match does not exist. To allow for comparisons, we arbitrarily chose $\tau \geq +6.0\%$ ($T_{\text{ARSS}} \geq 0.984$) as the performance benchmark. Spectral performance of simulated or fabricated components above this benchmark is considered within the target AR

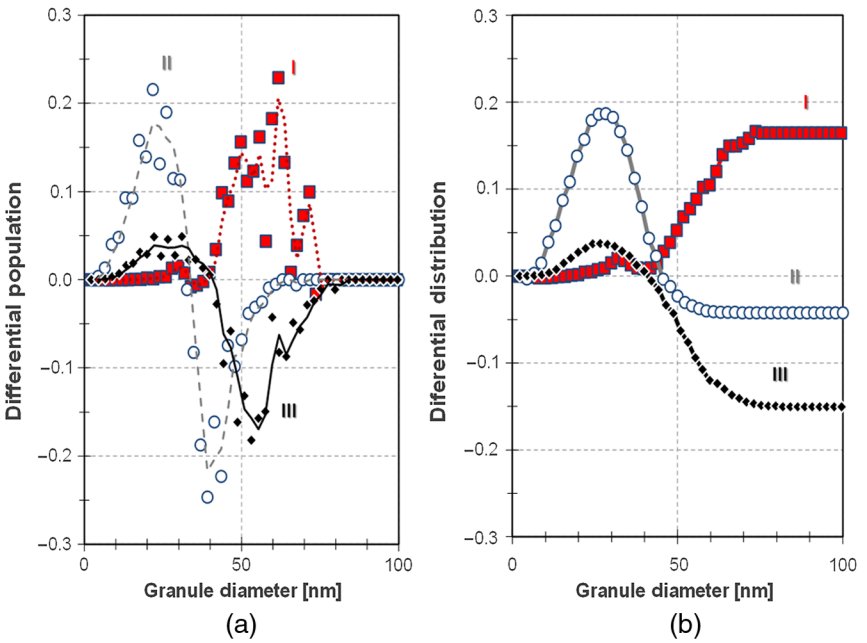

Fig. 3 Differential population (a) and differential normalized distribution (b) of the granule sizes measured from the FS sample random AR surfaces. The identifiers (I, II, and III) correspond to the measured process types from Table 1. Positive numbers indicate a plurality of silica islands, where negative numbers indicate more voids (air) than islands. The trend lines are for ease in viewing.

bandwidth. Data in Fig. 4 indicate that the PAR has an AR bandwidth of 340 nm, with peak performance ($\tau = +7.2\%$) at 633 nm. Of note is the gradual enhancement reduction of the PAR at wavelengths longer than 900 nm, whereas the short wavelength transmittance is sharply rising after 300-nm wavelength due to the single-layer design. A more detailed comparison of the transmission enhancement above 6%, namely the peak enhanced wavelength and the enhancement bandwidth, is shown in Table 2.

The rARSS samples tested (Fig. 4) demonstrated transmission enhancement ranging from $\tau = +6.1\%$ to $+6.9\%$, near the 633-nm wavelength. The different morphologies of the subwavelength structures, which depend on the process parameters, determined the broadband antireflective property and the optical performance of the surface. Sample A has the widest AR bandwidth. The highest transmission enhancement was measured using sample B, within an AR bandwidth of 575 nm, second highest in the set. As shown in Table 2, the asymmetrically processed sample C has the narrower enhanced bandwidth. Sample C has also the lowest transmission enhancement at 633 nm, compared with the other three FS rARSS substrates. Overall, the processed substrates show mutually comparable spectral transmission responses.

The polarized transmission measurements yielded the results shown in Fig. 5. The angular resolution of our measurements was ~0.1 deg, and multiple measurements were conducted for each AOI. The average maximum-to-minimum measurement deviation was <0.007% for all data points and the average standard deviation was <0.08% for all data points. The dynamic detection range of the CASI system is capable of resolving smaller deviations, which allows for high confidence in the measurements. All samples had higher polarized transmittance than the unprocessed FS, from 0 deg to 36 deg AOI. Sample B had the highest polarization insensitivity, with $T_p = T_s$ from 0 deg to 57 deg AOI. Sample C was found to be underperforming all rARSS substrates.

The fact that the samples processed with the same features on both sides (samples A, B, and D) showed polarization insensitivity from at least 0 deg to 30 deg AOI is comparable with both theoretical and experimental results found in the literature for periodic AR surface structures.[29,30] However, these periodic examples do not show polarization insensitivity near the Brewster's angle like sample B does here. Poitras and Dobrowolski[31] have shown that polarization insensitivity is possible to achieve at extreme angles of incidence using a

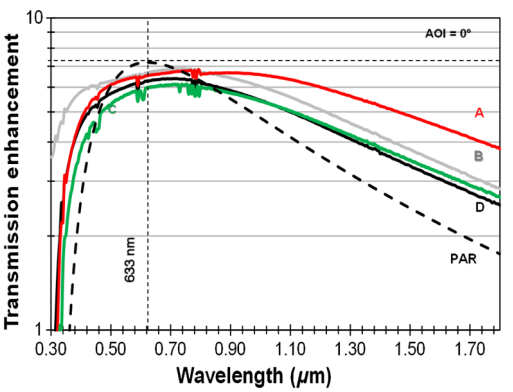

Fig. 4 Measured spectral transmission enhancement in percent (τ), for FS samples processed with rARSS on both sides. The four samples depicted by solid lines (A, B, C, and D) were etched as shown in Table 1. The transmission spectra were measured at normal incidence. The enhancement scale is logarithmic. The horizontal dashed line indicates the theoretical maximum transmission enhancement value for FS, and the vertical dashed line indicates the HeNe laser wavelength at 633 nm. The PAR simulation result is shown as the dashed line.

Table 2 Comparative performance list of the simulated ARC and fabricated rARSS on 1-mm-thick FS substrates.

Data type	Sample	$\tau > 6\%$ bandwidth (nm)	Peaked τ at wavelength (nm)	τ at peak wavelength (%)	τ at 633 nm wavelength (%)
Simulation	PAR	340	633	+7.2	+7.2
Fabricated	A	710	765	+6.8	+6.6
	B	575	760	+6.9	+6.7
	C	175	715	+6.1	+6.0
	D	310	710	+6.4	+6.3

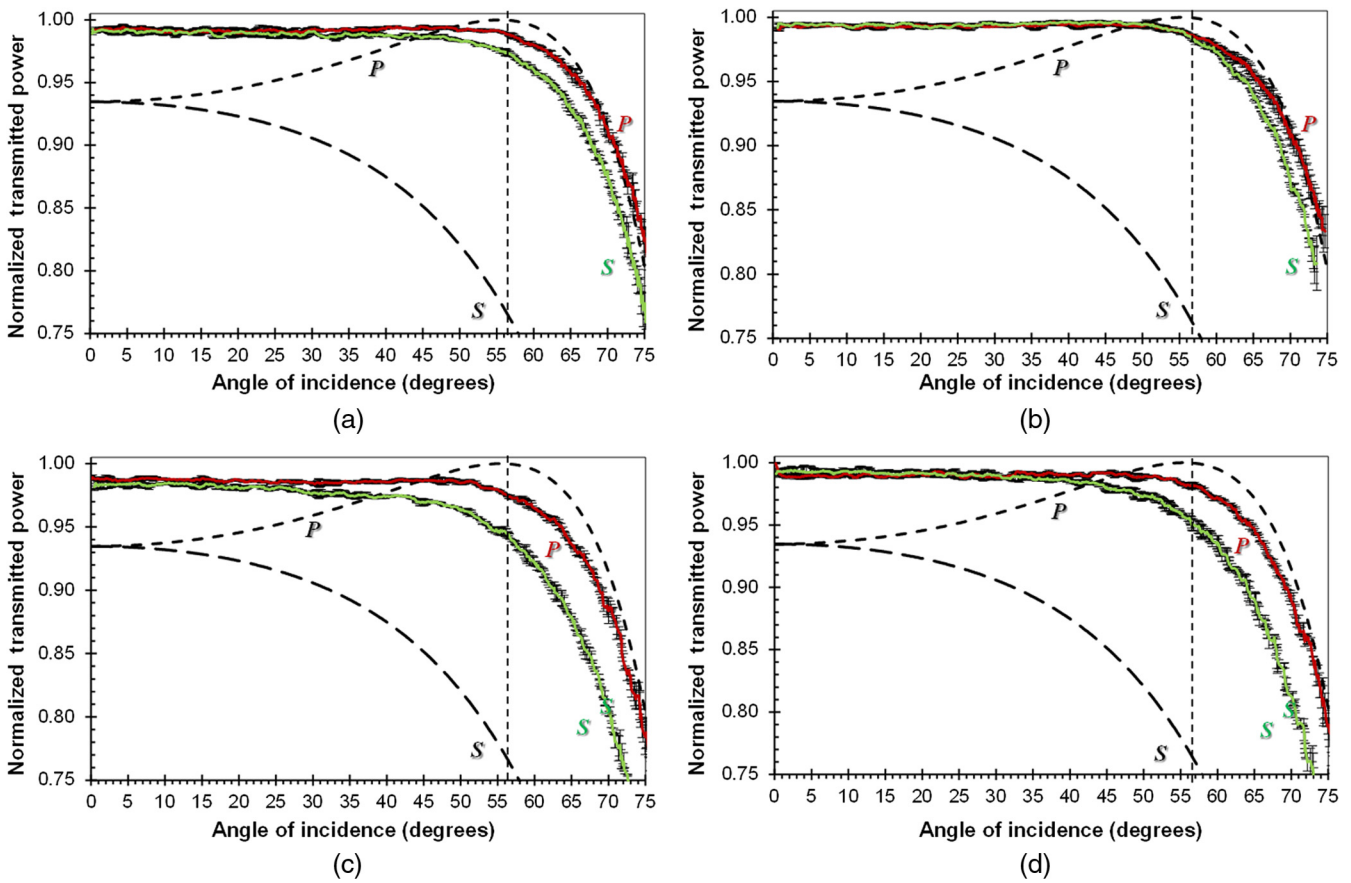

Fig. 5 Measured normalized transmitted power for *s* (green points) and *p* (red points) polarized light through both surfaces of the FS samples, taken at 633 nm. Dashed lines shown are the theoretical *S* and *P* transmission for an unprocessed FS slab. Brewster's angle (55.4 deg) is also indicated by the vertical dashed line. The labels A, B, C, and D correspond to the substrates listed in Tables 1 and 2. The maximum and minimum measurement values are indicated by the vertical limit bars for each AOI.

gradient refractive index with the appropriate refractive index profile. Since these rARSS are modeled as a gradient refractive index material, rather than as a subwavelength grating, which is the periodic AR surface structures standard model, it appears that this polarization independence ability can be understood as the result of a gradual index increment from the superstrate value to the substrate index value. It can also be assumed that rARSS that have different polarization independence performances must have different gradient refractive index profiles.

Sample A, which has the widest transmission enhancement bandwidth at normal incidence and a τ comparable with sample B, is polarization insensitive to about 50 deg AOI, with a measurable difference in polarized enhancement beyond that angle. Of note is the inability of all rARSS substrates to match the Brewster's angle transmittance for the *p*-polarized state, where the unprocessed substrate has a ~100% value. This can be interpreted as a physical manifestation of a silica "dilute" layer, conceptually equivalent to the EMA layer.

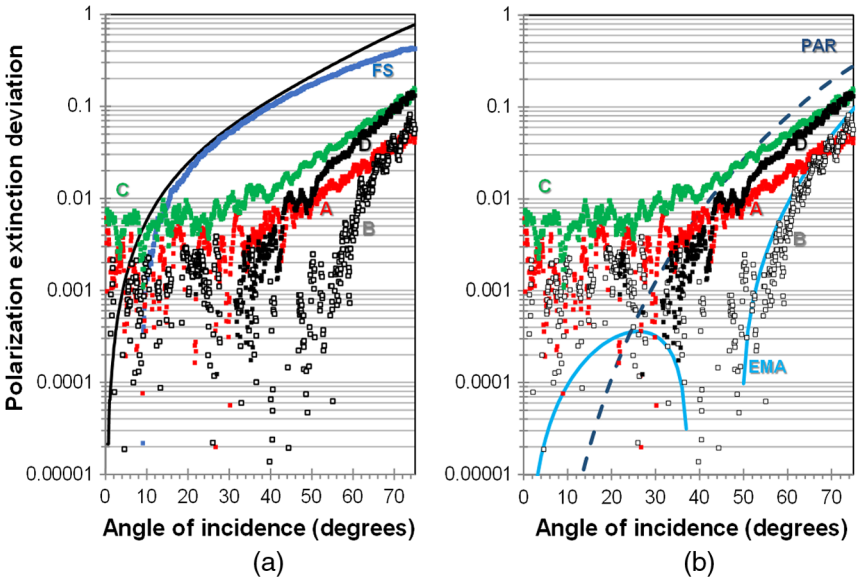

Fig. 6 (a) Semilog scale presentation of the polarization extinction ratio deviation for each measured sample and plain FS, as a function of angle of incidence at 633-nm wavelength. The solid black line is the theoretical value for unprocessed FS. (b) Computed polarization extinction ratio deviation data from (a) and the computed results for PAR and the EMA simulation of the rARSS surface.

To make a clear quantitative comparison of the polarized transmission response of the rARSS substrates, as mentioned previously, we calculated the deviation from unity of the polarization extinction coefficient. Figure 6(a) shows the results from the measured set A, B, C and D, where Fig. 6(b) shows the same results compared with the computed performance of the ideal PAR. Displaying the data obtained using Eq. (2) on a semilogarithmic scale allows for direct comparison of the polarization insensitivity, as the range of 0.1 to 0.0001 is magnified. The unprocessed FS substrate is also plotted for reference in Fig. 6(a).

Apart from the deviation of measured values for AOI $>$ 65 deg, the four rARSS samples have distinguishable performance traits. As the desired polarization independence is indicated by measurements as close to zero as possible, sample B is outperforming all other substrates. The B polarization extinction transmission ratio deviation from unity ($e_T - 1$) value from Fig. 6(a) is below 0.01 for AOI $<$ 61 deg. Substrates A and D, with different surface processing but identical processing on the front and back of the sample, show a similar value for AOI $<$ 50 deg, where substrate C bifurcates beyond 35 deg. Of note is the difference in the slope of $e_T - 1$ for A and D beyond 50 deg, an indication that the AR layers are not identical in nature. At low AOI $<$ 30 deg, the simulated PAR has better polarization insensitivity than the measured samples, mainly due to the absence of a limiting value for the simulation. The substrates A, D, and C have an extinction ratio deviation: $0.0001 < e_T - 1 < 0.01$, in the range of 0 deg and 30 deg. Tested sample B can be best simulated using a stratified EMA multilayer boundary, with conical random features of a maximum height of 400 nm and 40 sequential strata.

4 Conclusions

The four samples discussed in this paper show that rARSS with quantitatively different morphological features can have very similar transmission spectra at normal incidence. At normal incidence, these samples had peak transmission enhancement values comparable with PAR thin-film simulations. This could lead to the assumption that many different rARSS fabrication morphologies will act identically to each other and comparably to a PAR thin film. However, when the transmission through the rARSS samples is investigated at varying angles of incidence and with separate polarization states, differences between the various rARSS feature morphologies and their performance become apparent. Our results show that FS substrates processed with rARSS have high transmission enhancement for AOI of 0 deg to 55 deg, for the desired wavelength of performance. The rARSS samples were also shown to have a lower degree of polarization (measured on the order of 10^{-3}) than PAR thin-film simulations and polarization insensitivity from 0 deg to 60 deg. When the samples were compared with each other, our results show that samples with different feature morphologies on each side of the substrate will only have polarization insensitivity at low AOI. For samples with identical features on both sides of the substrate, some may perform similarly at low AOI, but they will eventually show two distinct polarization extinction deviation curves as AOI increases. Ultimately, the best performing rARSS sample (the sample with the polarization independence results as close to zero for the largest AOI possible) was the sample that was best simulated by an EMA multilayer boundary, which adds further validity to using this method for rARSS simulation in the future. These results can have considerable impact on the AR treatment of FS optical surfaces for polarization sensitive applications in the future.

Disclosures

The authors have no competing interests to declare.

Acknowledgments

The authors would like to thank the UNC Charlotte Center for Optoelectronics and Optical Communications for the use

of the CASI scatterometer and the microfabrication clean room facilities. They would also like to thank the Science, Mathematics, and Research for Transformation (SMART) scholarship for financially supporting Abigail Peltier in graduate school.

References

1. T. Aytug et al., "Monolithic graded-refractive-index glass-based antireflective coatings: broadband/omnidirectional light harvesting and self-cleaning characteristics," *J. Mater. Chem. C* **3**, 5440–5449 (2015).
2. U. Schulz et al., "Gradient index antireflection coatings on glass containing plasma-etched organic layers," *Opt. Mater. Express* **5**, 1259 (2015).
3. P. Shang et al., "Disordered antireflective subwavelength structures using Ag nanoparticles on fused silica windows," *Appl. Opt.* **53**, 6789–6796 (2014).
4. S. Chattopadhyay et al., "Anti-reflecting and photonic nanostructures," *Mater. Sci. Eng. R Rep.* **69**(1), 1–35 (2010).
5. D. S. Hobbs, B. D. MacLeod, and J. R. Riccobono, "Update on the development of high performance anti-reflecting surface relief microstructures," *Proc. SPIE* **6545**, 65450Y (2007).
6. L. E. Busse et al., "Anti-reflective surface structure for spinel ceramics and fused silica windows, lenses, and optical fibers," *Opt. Mater. Express* **4**(12), 2504–2515 (2014).
7. L. E. Busse et al., "Antireflective surface structures on optics for high energy lasers," *Proc. SPIE* **8959**, 89591L (2014).
8. W. H. Lowdermilk and D. Milam, "Graded-index antireflection surfaces for high-power laser applications," *Appl. Phys. Lett.* **36**, 891–893 (1980).
9. D. A. Boyd et al., "Superhydrophobic, infrared transmissive moth eye-like substrates for use in wet conditions," *Proc. SPIE* **10179**, 1017906 (2017).
10. D. A. Boyd et al., "Modification of nanostructured fused silica for use as superhydrophobic, IR-transmissive, anti-reflective surfaces," *Opt. Mater.* **54**, 195–199 (2016).
11. H. A. Macleod, *Thin Film Optical Filters*, 3rd ed., Institute of Physics Publishing, Philadelphia, Pennsylvania (2001).
12. D. H. Raguin and G. M. Morris, "Antireflection structured surfaces for the infrared spectral region," *Appl. Opt.* **32**, 1154–1167 (1993).
13. E. B. Grann, M. G. Moharam, and D. A. Pommet, "Optimal design for antireflective tapered two-dimensional subwavelength grating structures," *J. Opt. Soc. Am.* **A12**, 333–339 (1995).
14. A. Sharma, D. V. Kumar, and A. K. Ghatak, "Tracing rays through graded-index media: a new method," *Appl. Opt.* **21**, 984–987 (1982).
15. J. A. Dobrowolski et al., "Toward perfect antireflection coatings: numerical investigation," *Appl. Opt.* **41**, 3075–3083 (2002).
16. A. K. Sood et al., "Development of large area nanostructure antireflection coatings for EO/IR sensor applications," *Proc. SPIE* **9609**, 96090D (2015).
17. T. Maier et al., "Antireflective surface structures in glass by self-assembly of SiO_2 nanoparticles and wet etching," *Opt. Express* **21**, 20254–20259 (2013).
18. B. Zollars et al., "Performance measurements of infrared windows with surface structures providing broadband, wide-angle, antireflective properties," *Proc. SPIE* **8708**, 87080Q (2013).
19. G. A. Niklasson, C. G. Granqvist, and O. Hunderi, "Effective medium models for the optical properties of inhomogeneous materials," *Appl. Opt.* **20**, 26–30 (1981).
20. D. A. G. Bruggeman, "The calculation of various physical constants of heterogeneous substances. I. The dielectric constants and conductivities of mixtures composed of isotropic substances," *Ann. Phys. (Leipzig)* **416**, 636–664 (1935).
21. S. Chen et al., "Cleaning multilayer dielectric pulse compressor gratings with top layer of HfO 2 by Piranha solution," *High Power Laser Part Beams* **23**(8), 2106–2110 (2011).
22. D. Dalacu and L. Martinu, "Optical properties of discontinuous gold films: finite-size effects," *Opt. Soc. Am. B* **18**(1), 85–92 (2001).
23. S. Norrman and T. Andersson, "Quantitative evolution studies of particle separation, size and shape for vapour-deposited ultrathin gold films on glass substrates," *Thin Solid Films* **77**, 359–366 (1981).
24. A. Peltier et al., "Control of spectral transmission enhancement properties of random anti-reflecting surface structures fabricated using gold masking," *Proc. SPIE* **10115**, 101150B (2017).
25. M. Schulze et al., "New approach for antireflective fused silica surfaces by statistical nanostructures," *Proc. SPIE* **6883**, 68830N (2008).
26. E. R. Dougherty and R. A. Lotufo, *Hands-on Morphological Image Processing*, SPIE Press, Bellingham, Washington (2003).
27. R. E. Fisher, B. Tadic-Galeb, and P. R. Yoder, *Optical System Design*, 2nd ed., p. 536, McGraw-Hill Publishers, New York (2008).
28. P. Yeh, *Optical Waves in Layered Media*, Chapter 5, John Wiley & Sons, Inc., Hoboken, New Jersey (2005).
29. D. G. Stavenga et al., "Light on the moth-eye corneal nipple array of butterflies," *Proc. Biol. Sci.* **273**, 661–667 (2006).
30. K. C. Park et al., "Nanotextured silica surfaces with robust superhydrophobicity and omnidirectional broadband supertransmissivity," *ACS Nano* **6**, 3789–3799 (2012).
31. D. Poitras and J. A. Dobrowolski, "Toward perfect antireflection coatings. 2. Theory," *Appl. Opt.* **43**, 1286–1295 (2004).

Abigail Peltier is a graduate student at UNC Charlotte, pursuing her doctorate in optical science and engineering. She received her bachelor's degree in physics from Bucknell University in 2011 and her master's degree in optical science and engineering from UNC Charlotte in 2015. In 2016, she was awarded the Science, Mathematics, and Research for Transformation (SMART) Scholarship.

Gopal Sapkota received his PhD from the University of North Texas, Denton, Texas, in 2014. He is an instructor of physics at Tri-County Technical College, Pendleton, South Carolina. He had worked as a postdoctoral fellow at University of North Carolina at Charlotte before moving to Tri-County College. His research interests are in nanostructure growth, characterization, and their application in optoelectronics.

Jason R. Case received his doctorate from the Department of Physics and Optical Science at UNC Charlotte in 2015. He is a senior optical tooling engineer in the Optical Tooling Department at Johnson and Johnson Vision. Previously, he was a postdoctoral researcher at UNC Charlotte where his principal work was centered on the properties of high-energy laser materials. His research interests include precision metrology, diamond point turning, thermography, and optical material properties.

Menelaos K. Poutous received his doctorate from the School of Physics at the Georgia Institute of Technology in 1996. He is an assistant professor in the Department of Physics and Optical Science, UNC Charlotte. He previously held a principal development engineer's position at Digital Optics Corporation, and before that he was a lecturer in physics at Emory University. His research interests are in spectroscopy, diffractive micro-optical elements, photo-lithographic fabrication, and artificial optical surfaces.